High-Resolution Phase Sampled Interferometry Using Symmetrical Number Systems

Phillip E. Pace, *Senior Member, IEEE*, David Wickersham, David C. Jenn, *Senior Member, IEEE*, and Nathan S. York

***Abstract*—This paper identifies a new phase sampling interferometer approach that can be easily incorporated into the established techniques to provide a high resolution, small-baseline array with fewer number of phase sampling comparators. The approach is based on preprocessing the received signal using symmetrical number systems (SNS). Antennas based on both an optimum symmetrical number system (OSNS) and a robust symmetrical number system (RSNS) are investigated. The SNS preprocessing is used to decompose the spatial filtering operation into a number of parallel suboperations (moduli) that are of smaller computational complexity. A much higher direction finding (DF) spatial resolution is achieved after the N different moduli are used and the results of these low precision suboperations are recombined. By incorporating the OSNS or RSNS preprocessing concept, the field of view of a specific configuration of interferometers and phase sampling comparator arrangements can be analyzed exactly. The OSNS gives the maximum dynamic range or number of spatial resolution bins while the RSNS reduces considerably the number of possible encoding errors. Experimental results for both a 5-bit OSNS and a 6-bit RSNS array are compared. The errors in the encoding of the direction of arrival are quantified for both architectures.**

***Index Terms*—Directional finding, electronic warfare, symmetrical number system.**

I. Introduction

DIRECTION finding (DF) systems find applications in many disciplines including geolocation, navigation and targeting for weapon systems. They are also used for tracking by law enforcement, military personnel, and wildlife management. Radio DF systems commonly use phase sampled linear interferometer arrays to measure the direction of arrival of a single incident planar waveform in order to estimate the geographical bearing of the emitter. Each interferometer consists of two receive elements separated by a distance d (baseline). A waveform impinging on an ideal interferometer has the *same* amplitude at both element locations. Thus, all of the information about the direction of arrival is contained in the phase of the signal measured by the different array elements. Consequently, most existing radio DF systems are based on phase only measurements. As the planar waveform impinges upon the receive elements, the difference in phase is sampled (by several comparators) and indicates the direction of arrival. Ambiguities in the direction of arrival occur if the separation between interferometer elements is greater than half the electrical wavelength.

To resolve the ambiguities, the addition of a second interferometer, can be used [1]. Multiple baseline systems, however, can become quite long when high resolution is required. Many approaches to resolving the ambiguities within a phase sampling system have been recently investigated. The *extended phase interferometry* technique to resolve the ambiguities incorporates both calibrated phase and amplitude response data from the antenna arrays [2]. This is done by appropriately weighting the square of the baseline phase differences with the antenna gains. The incorporation of amplitude data provides significant performance improvement over phase only interferometry, however, it requires a modest increase in computational complexity. *Pseudo Doppler* techniques have also been investigated in the 2–2000 MHz range [3]. In this approach, the system employs a circular array of four omni-directional antennas. A commutation switch samples the antennas such that the resulting phase modulation on the received signal encodes the direction of arrival. As the elements are commutated an FM discriminator responds with impulses with size approximately proportional to the phase step between each element. The maximum spacing between adjacent elements is less than half a wavelength. The phase of the output is used to quantize an estimated angle of arrival. The single channel interferometer minimizes cost and power consumption by avoiding a multitude of expensive receivers and by employing the cost effective pseudo Doppler antenna. The symmetric pair antenna array provides accurate DF by means of low resolution phase measurements, achieved by virtue of the symmetry of the array geometry [4]. This type of array consists of pairs of antenna elements that are arranged around a common phase center. Due to symmetry, any arriving wavefront generates a phase lead at one member and a phase lag of equal magnitude at the other member of the symmetric pair. Since the polarity of the output signal is dependent on the angle of incidence, it can be used to determine the signal's angle of arrival. The sign bit pattern of the pairs of a given symmetric pair array will change for different angles of incidence and assuming an unambiguous arrangement (annular zones on the surface of a sphere) must be distinguishable.

This paper identifies a new phase sampling interferometer approach that can provide a high resolution, small baseline array with fewer number of phase sampling comparators. The approach is based on preprocessing the received signal using symmetrical number systems (SNS). Antennas based on both an optimum symmetrical number system (OSNS) and a robust symmetrical number system (RSNS) are investigated. The SNS pre-

Manuscript received May 2, 2000; revised January 29, 2001. This work was supported in part by Naval Research Laboratory and in part by the Naval Postgraduate School Center for Reconnaissance Research.

The authors are with the Department of Electrical and Computer Engineering, Naval Postgraduate School, Monterey, CA 93943 USA.

Publisher Item Identifier S 0018-926X(01)06369-4.

processing is used to decompose the spatial filtering operation into a number of parallel suboperations (moduli) that are of smaller computational complexity. Each suboperation is a separately configured interferometer that symmetrically folds the detected phase difference with folding period equal to the twice the modulus $2m_i$ (for the OSNS) and $2Nm_i$ (for the RSNS) where N is the number of interferometers that are used within the linear array. A small comparator ladder midlevel quantizes each folded phase response. Consequently, each suboperation only requires a precision in accordance with that modulus. A much higher DF spatial resolution is achieved after the N, different moduli are used and the results of these low precision suboperations are recombined. By incorporating the OSNS or RSNS preprocessing concept, the field of view of a specific configuration of interferometers and phase sampling comparator arrangements can be analyzed exactly. The OSNS gives the maximum dynamic range or number of spatial resolution bins while the RSNS reduces considerably the number of possible encoding errors. Experimental results for both a 5-bit OSNS and a 6-bit RSNS array are compared. The errors in the encoding of the direction of arrival are quantified for both architectures.

The outline of this paper is as follows. In Section II, two-element interferometry is briefly reviewed. In Section III, the OSNS is presented and the practical implications of building the OSNS DF antenna are addressed. Experimental results are shown to demonstrate the transfer function of the array and quantify the possible encoding errors. Section IV presents the RSNS and the design equations for the RSNS array. Experimental results are also shown for comparison. It is shown that although the RSNS has a somewhat smaller dynamic range than the OSNS, the absence of encoding errors makes it particularly attractive for modern DF systems.

II. Phase Sampled Interferometery and Folding Waveforms

A two element linear interferometer is shown in Fig. 1. The two antenna elements are spaced a distance d apart and the incident plane wave arrives with bearing angle θ_B. In this phase monopulse configuration the angle θ_B is measured from the perpendicular to the baseline axis and can take on values $\pi/2 > \theta_B > -\pi/2$. The phase difference between the two elements is

$$\Delta\psi = \psi_1 - \psi_2 = \frac{2\pi}{\lambda} d\sin(\theta_B) \tag{1}$$

and is a function of the incidence angle of the wave.

The signals received by the antenna elements are mixed (multiplied together and lowpass filtered) resulting in an output signal whose frequency is the difference of the two input signal frequencies. Because the signals have the same frequency, the mixer output voltage is a value proportional to the difference between signal phases ψ_1 and ψ_2. This difference is not purely $\Delta\psi$ because of the time delays due to the different transmission line lengths from each antenna element. However, these line lengths are known and can be compensated for in the angle estimate. Let the signals from the two antenna elements be

$$v_1(t) = V\cos[2\pi ft + \phi_1(t)] \tag{2}$$

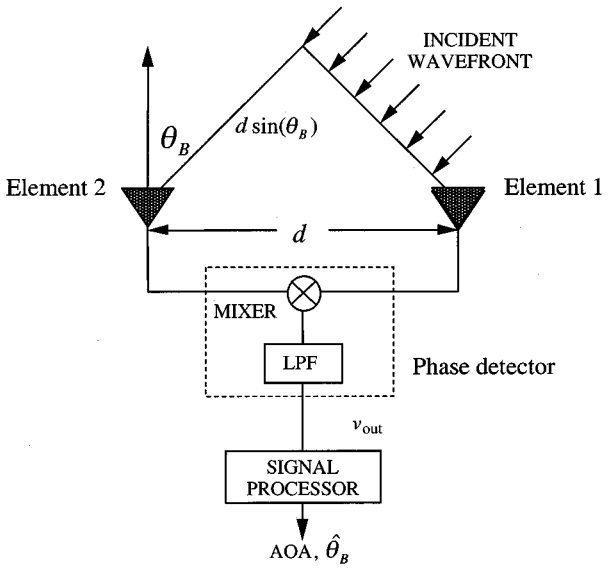

Fig. 1. Linear two element interferometer array geometry.

and

$$v_2(t) = V\cos[2\pi ft + \phi_2(t)] \tag{3}$$

where V is the maximum value of the voltage at the antenna elements. Let ψ_0 be the phase difference between the transmission lines to the two elements. The low-pass mixer output voltage is

$$v_{\text{out}} = \frac{V^2}{2}\cos(\Delta\phi) = \frac{V^2}{2}\cos\left(\frac{2\pi d}{\lambda}\sin(\theta_B) + \psi_0\right) \tag{4}$$

which contains the plane wave angle of arrival (AOA) information. For values of $d = \lambda/2$ and $\psi_0 = 0$, $\Delta\phi = \pi\sin(\theta_B)$. As the AOA θ_B varies from $-\pi/2$ to $\pi/2$, the phase difference $\Delta\phi$varies from $-\pi$ to π as shown in Fig. 2(a). The output voltage from the phase detector is also a function of the phase difference and is a symmetrical folding periodic waveform. Together these relationships give the phase detector output voltage as a symmetrical function of the AOA as shown in Fig. 2(b) for $d = \lambda/2$.

Ambiguities are generated for baselines where $d > \lambda/2$. That is, the phase detector output voltage is highly ambiguous with a single phase corresponding to many angles of arrival. The number of folding periods n that occur within an AOA of π radians is

$$n = \frac{2d}{\lambda}. \tag{5}$$

For example, with $d = 7.5\lambda$, $n = 15$ folds are available as shown in Fig. 3. The folding period is not constant but grows larger in proportion to the angle off broadside because of the $\sin(\theta_B)$dependence in (4).

The ambiguities within the symmetrical folding waveforms represent the phase difference between the elements and can be resolved by using additional interferometers in the linear array. Typically, each interferometer in the linear array symmetrically folds the phase response with the folding period between interferometers being a successive factor of two or $d_4 = 2d_3 = 4d_2 = 8d_1$. High speed binary comparators are used to produce

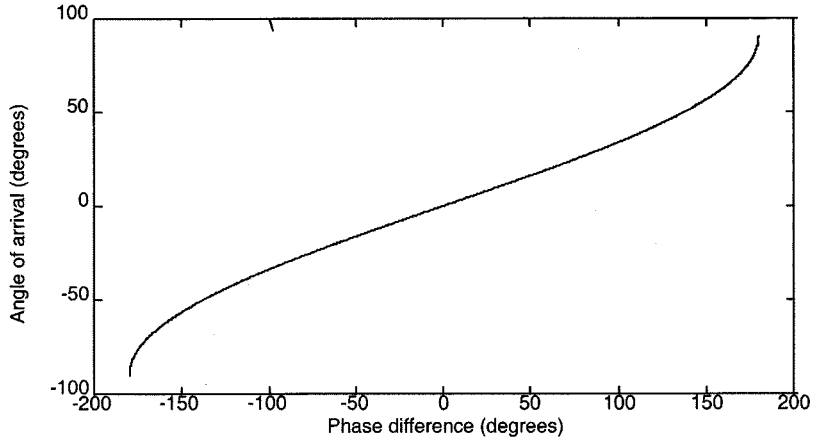

(a)

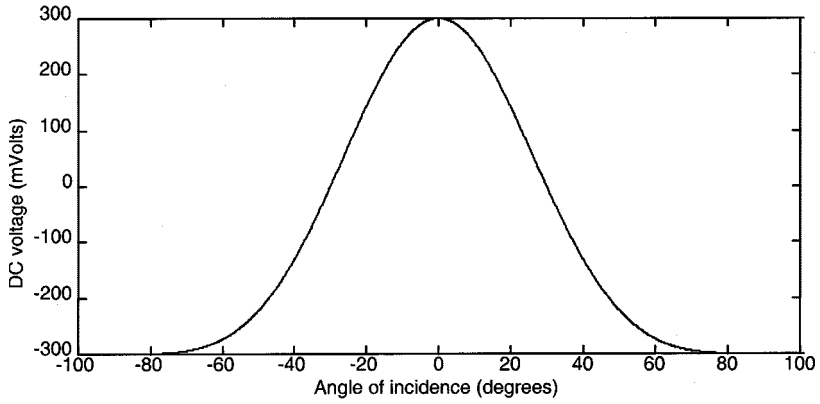

(b)

Fig. 2. Two-element interferometry with $d = \lambda/2$. (a) Mixer output voltage versus phase difference between two elements. (b) Mixer output voltage versus angle of incidence.

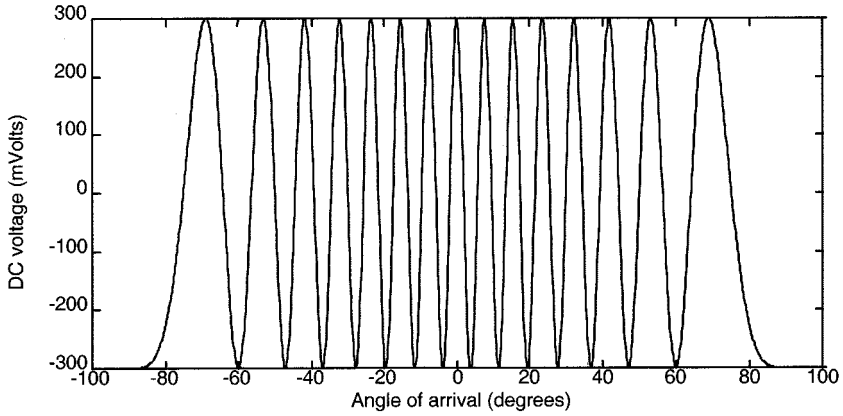

Fig. 3. Mixer output voltage versus AOA for $d = 7.5\lambda$.

a digital output. The folding waveforms are shifted appropriately using a phase shifter in each channel to achieve a Gray code result. The folded output from each phase detector is then quantized with a single comparator with a normalized threshold level $T = 0.5$. Together, the comparator outputs directly encode the signal's AOA in the Gray code format. This approach makes use of the periodic dependence of the interferometer's phase response on the applied plane wave's AOA and the distance between the elements of each interferometer. One of the major limitations associated with this approach is the achievable resolution. For the folding periods to be a successive factor of 2, the distance between the elements must also be doubled. That is, an 8-bit DF antenna using the previous scheme would require element spacings $\lambda/4$, $\lambda/2$, λ, 2λ, $4\lambda, \ldots,$ 32λ with a total baseline length of 32λ. This distance doubling of the element spacings requires complex analog hardware and adversely affects the physical implementation of the DF architecture and ultimately constrains the achievable resolution.

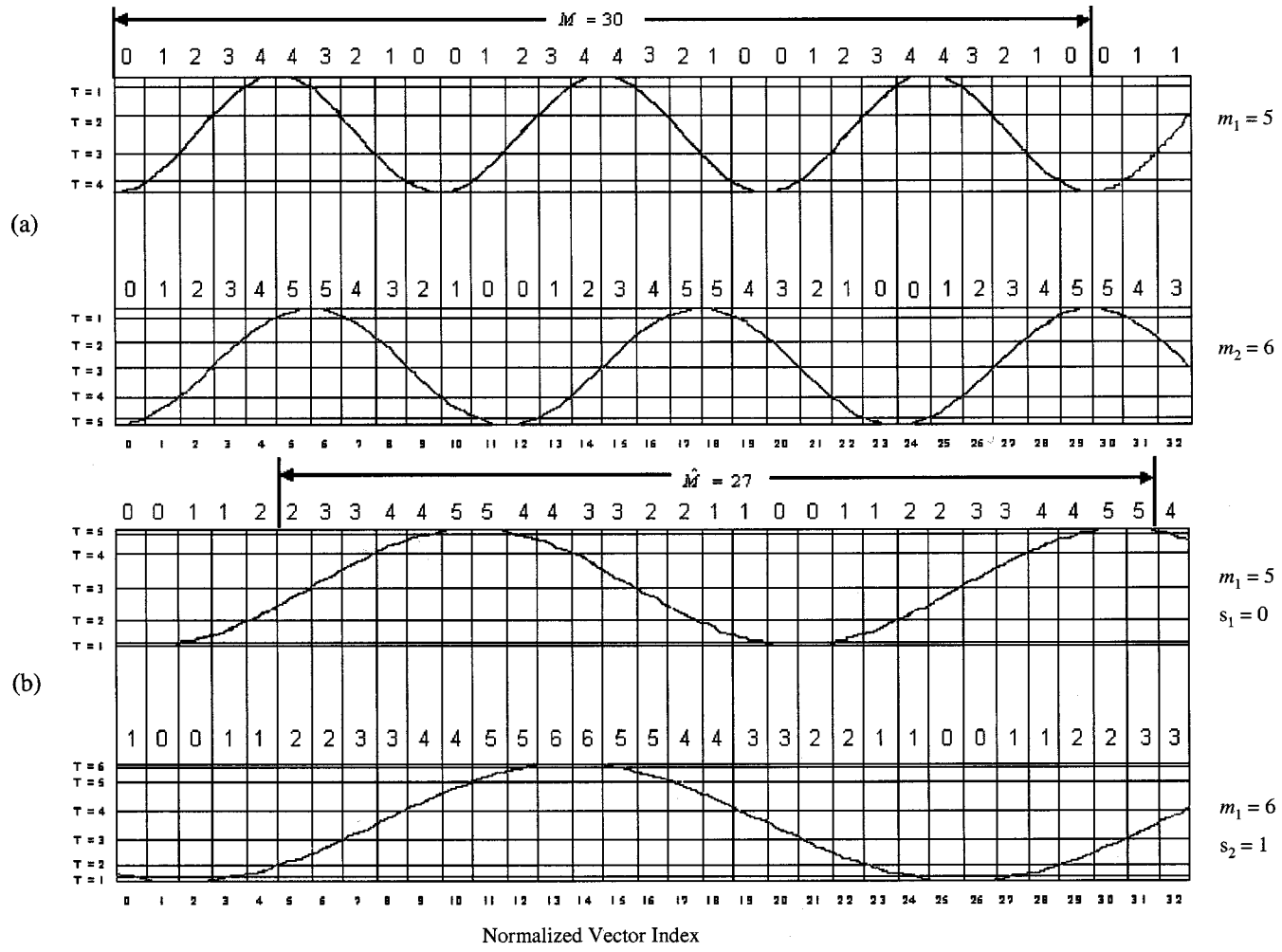

Fig. 4. Folding waveforms and integer values within moduli $m_1 = 5$ and $m_2 = 6$. (a) The OSNS. (b) The RSNS.

III. The OSNS DF Antenna

Incorporation of the OSNS encoding overcomes the major limitations of the binary encoding approach and provides an efficient method to enhance the resolution of the array while minimizing the total baseline. The OSNS provides an efficient solution by using additional baselines to correct ambiguities in the first baseline using multilevel quantization and prime sequences to obtain uniqueness over the dynamic range.

A. Optimum Symmetrical Number System

The OSNS is composed of a number of pairwise relatively prime (PRP) moduli m_i. The integers within each OSNS modulus are representative of a symmetrically folded waveform with the period of the waveform equal to twice the modulus, i.e., $2m_i$ [5]. For m given, the row vector below gives the integer values within twice the modulus

$$\overline{x}_m = [0, 1, \ldots, m-1, m-1, \ldots, 1, 0]. \tag{6}$$

Fig. 4(a) shows part of the OSNS folding waveforms and the integer values within the modulus for $m_1 = 5$ and $m_2 = 6$. The horizontal axis represents the normalized input. The vertical lines represent folding waveform reference levels. The numbers at the top of the figure represent the number of reference levels that are crossed by the folding waveform for a given input value. The period of one complete fold is equal to $2m_1 = 10$ and $2m_2 = 12$.

Due to the presence of ambiguities, the integers within the vector derived by (6) do not form a complete system of length $2m$ by themselves. The ambiguities that arise within the modulus are resolved by considering the paired values from all channels together. If N pairwise relatively prime moduli are used, the dynamic range (the number of unambiguous vectors) of this scheme is [6]

$$M = \prod_{i=1}^{N} m_i. \tag{7}$$

This dynamic range is also the position of the first repetitive moduli vector. As shown in Fig. 4(a), the dynamic range for the $m_1 = 5$ and $m_2 = 6$ case is $M = 30$. That is, no set appears twice for a normalized input in the range [0, 29].

B. OSNS Antenna Architecture

Fig. 5 shows the schematic diagram of an $N = 2$ channel OSNS DF antenna. The array consists of three elements with all channels sharing a common element. With the proper distances between elements, each interferometer folds the phase

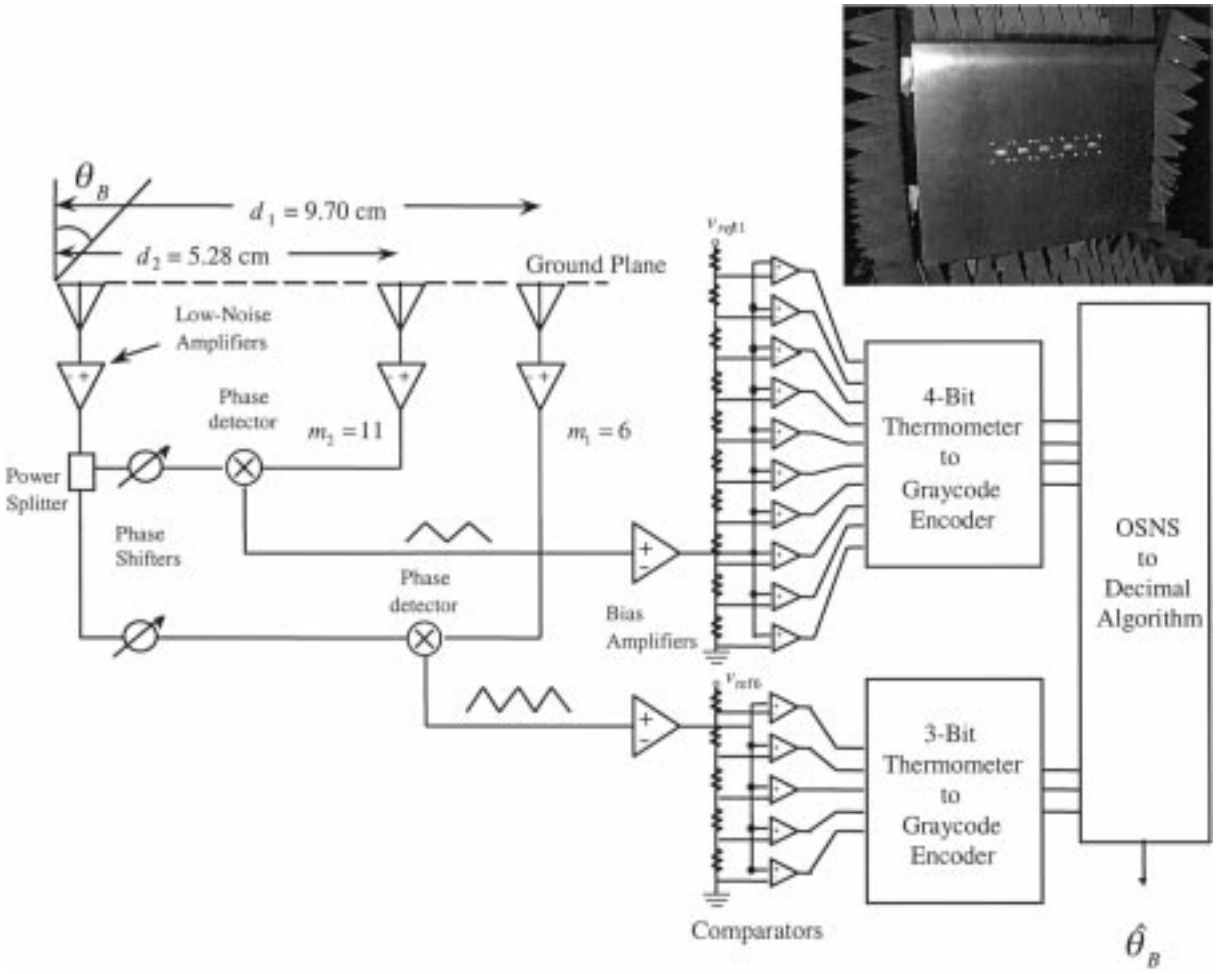

Fig. 5. Schematic diagram of the OSNS array with $m_1 = 6$ and $m_2 = 11$.

response at $2m_i$. The phase response from each channel is quantized using $m_i - 1$ comparators. The integers shown on top of both folding waveforms in Fig. 4(a) represent the number of comparators ON due to the phase voltage exceeding the comparator matching threshold voltage.

The distance between each pair of elements is a function of the modulus, m_i. The phase response must have the correct number of folds to cover the dynamic range. For a given modulus m_i, the number of folds within the dynamic range is

$$n_i = M/2m_i. \tag{8}$$

Since each fold of the array corresponds to a change in phase of π for $d = \lambda/2$, the required spacing between the reference element and the respective element of channel i is given by

$$d_i = n_i \frac{\lambda}{2} = \frac{M\lambda}{4m_i}\xi. \tag{9}$$

The bin widths are uniform in size in $\sin(\theta_{\mathrm{B}})$ space with a width $2/M$. Therefore, the spatial resolution is given by

$$r_k = \arcsin\left(\frac{2k - M + 2}{\xi M}\right) - \arcsin\left(\frac{2k - M}{\xi M}\right) \tag{10}$$

where $k \in \{0, 1, \ldots M - 1\}$ and $k = 0$ is the bin that starts at $\theta_B = -\pi/2$. The variable ξ is a scale factor that can be used to compress the encoded field of view symmetrically about broadside. The phase waveforms are not ideal over 180° because of the element pattern degradation at wide angles. Since the waveforms at wide angles are not usable, the SNS can be remapped to the usable portion of the waveform to increase resolution. The scale factor is defined to be

$$\xi = \frac{d'}{d} = \frac{\sin(\theta)}{\sin(\theta')} \tag{11}$$

where θ corresponds to phase angle for the unscaled configuration and θ' is the desired phase angle for the compressed configuration. Note that the spatial resolution is not uniform over the range of $-\pi/2$ to $\pi/2$. The resolution is finer than r at broadside ($\theta = 0°$) and increases with angle off broadside, because of the $\sin(\theta_B)$ dependence in (5).

C. Experimental Results

A linear array based on the moduli $m_1 = 6$ and $m_2 = 11$ was designed, fabricated, and tested at a frequency 8.5 GHz. The radiating elements are open-ended waveguides as shown in Fig. 5. For moduli $m_1 = 6$ and $m_2 = 11$, $d_1 = 9.70$ cm and $d_2 = 5.28$ cm. With $M = 66$, the number of folding periods $n_1 = 5.5$ and $n_2 = 3$. To provide an adequate signal-to-noise ratio, a low-noise amplifier is included at the output of each interferometer element. Since the common element splits the

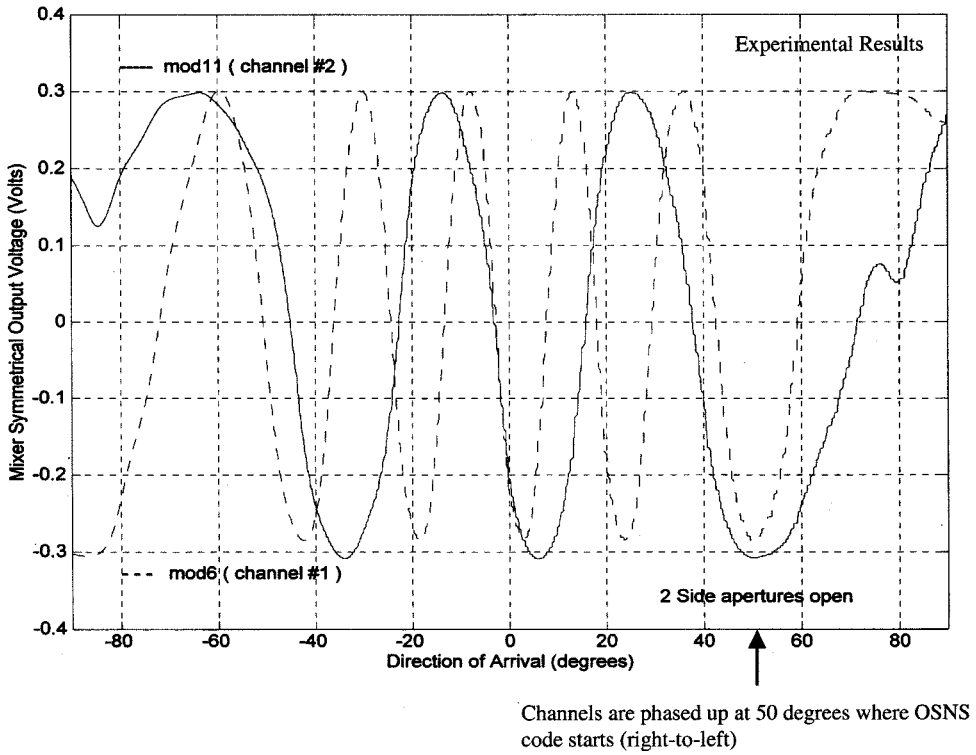

Fig. 6. Measured mixer output voltages for the OSNS array.

signal into N paths, an attenuator is placed in the other branches to balance the amplitudes. The amplifiers operate in saturation so that the mixer input signal levels are independent of the angle of incidence. A fixed phase shifter is also included in one branch of each interferometer so that the symmetrically folded phase response waveforms from each mixer may be aligned. This alignment insures that the comparators in the digital processor properly sample the phase waveform and encode it in the OSNS.

The anechoic chamber facility at the Naval Postgraduate School was used for the antenna pattern measurements for each pair of elements. The measured mixer outputs are shown in Fig. 6. Since the array is not useful in the endfire regions, the phase response from each channel was minimized at an input AOA of -50°. This is the point where the digital code starts. Introducing the appropriate phase shifts at a point between the elements and the mixer controls the locations of the voltage minima. A simulation of the transfer function for the OSNS array is shown in Fig. 7(a) for $\xi = 1$. The measured transfer function (output of digital hardware) is shown in Fig. 7(b).

The spikes in the transfer function are AOA encoding errors. The phase waveforms must cross the comparator thresholds (code transitions) at the same time for all channels. The OSNS can present a problem at each of these specific AOAs. When some comparators, at positions to change, *do change*, while others do not, the recovered amplitude will have a large error. Encoding errors can also occur due to imperfections in the transmission line phases. These errors however, can be isolated with additional comparators and corrected using interpolation circuits as described in [6]. An alternate approach, however, is to develop a symmetrical number system that eliminates the possibility of this type of encoding error. That is, a symmetrical number system where only one comparator threshold is crossed at any one particular code transition.

IV. The RSNS Antenna

The RSNS preprocessing architecture is a modular scheme in which the integer values within each modulus (comparator states), when considered together, change *one at a time* at the next position (Gray code properties) [7]. Although the observed dynamic range of the RSNS is less than that of the OSNS given in (7), the RSNS Gray code properties make it particularly attractive for error control. With the RSNS preprocessing, the encoding errors due to comparator thresholds not being crossed simultaneously are eliminated. As a result, the interpolation circuits can be removed and only a small number of comparators are required.

A. The Robust Symmetrical Number System

In the RSNS, N different periodic symmetrical waveforms are used with pairwise relatively prime integers $m_1, m_2, \ldots, m_N$. The RSNS is based on the following sequence:

$$\overline{x}_{ml} = [0, 1, 2, \ldots, m-1, m, m-1, \ldots, 2, 1] \qquad (12)$$

where $\overline{x}_{ml}$ is a row vector and m is a positive integer ($m > 0$). In an N-channel RSNS, where $N \geq 2$, the basic sequence for the ith channel (modulus m) is

$$\overline{x}_{ml} = [0, 0, \ldots, 0, 0, 1, 1, \ldots, 1, 1, \ldots, m \\ m, \ldots, m, m, \ldots, 1, 1, \ldots, 1, 1]. \qquad (13)$$

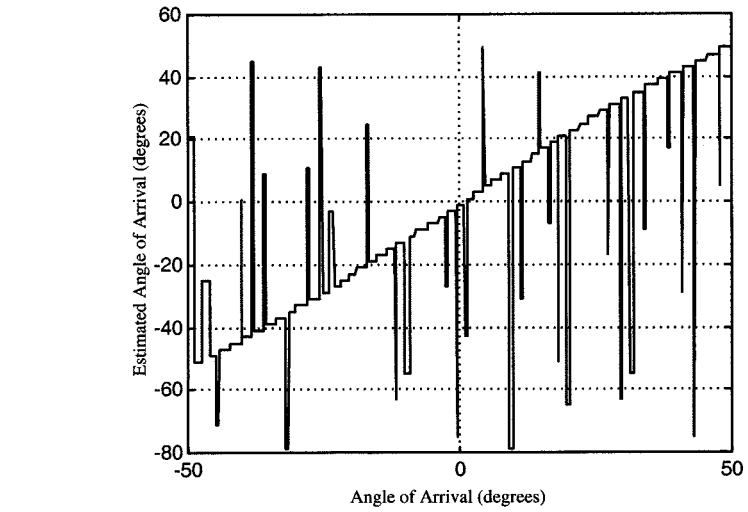

(a)

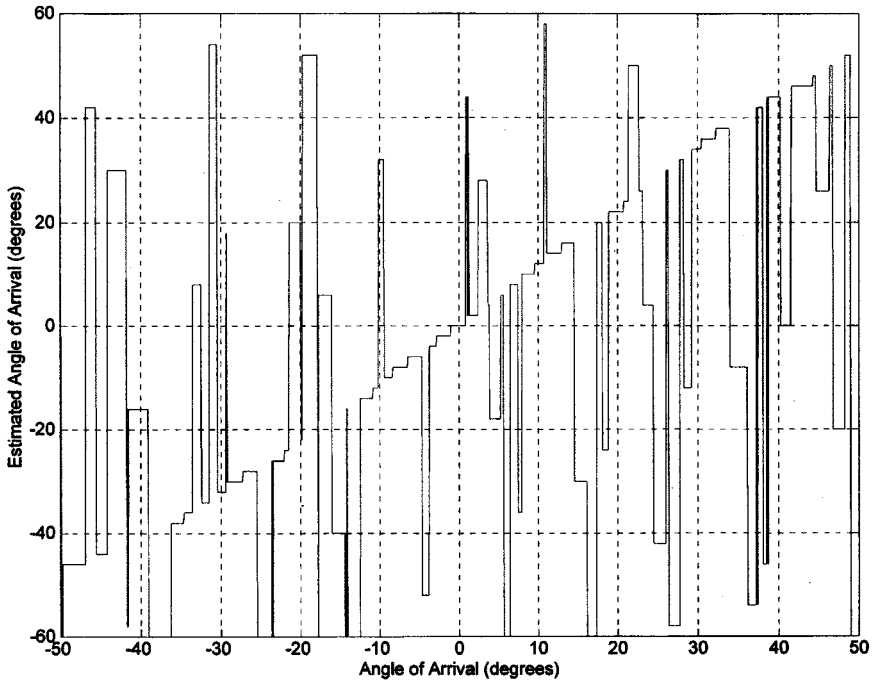

(b)

Fig. 7. Transfer function for the OSNS array. (a) Simulation. (b) Measured results.

In this sequence each value in the $\overline{x}_{ml}$ row vector is put N times in succession. This sequence is repeated in both directions, forming a periodic sequence with the period

$$P_{\mathrm{RSNS}} = 2mN. \tag{14}$$

Considering a single channel, the discrete states of the robust symmetrical number system can be expressed as

$$g = \begin{cases} \left\lfloor \dfrac{n - s_i}{N} \right\rfloor, & s_i \le n \le Nm_i + s_i + 1 \\ \left\lfloor \dfrac{2Nm_i + N - n + s_i - 1}{N} \right\rfloor & \\ & Nm_i + s_i + 2 \le n \le 2Nm_i + s_i - 1 \end{cases} \tag{15}$$

where

- g nth term of channel i;
- m_i channel modulus;
- s_i corresponding sequence shift $s_i \equiv 0, 1, 2, \ldots, N-1 \pmod N$ and $N \ge 2$ is the number of channels in the system.

The values $\{s_1, s_2, \ldots, s_N\}$ must form a complete residue system modulo N. Because of the relative property of the shifts, one of the shift values will be set equal to 0. The index n corresponds to the input value. The discrete states of the RSNS are indexed using the $s_i = 0$ row vector with the index starting from the first zero. Note that the largest integer within each periodic sequence is the modulus m.

An N-channel RSNS is formed of vectors by picking N moduli m_i and N shift values s_i, $1 \le i \le N$. Since the fundamental period for channel i is $2Nm_i$, it follows that the

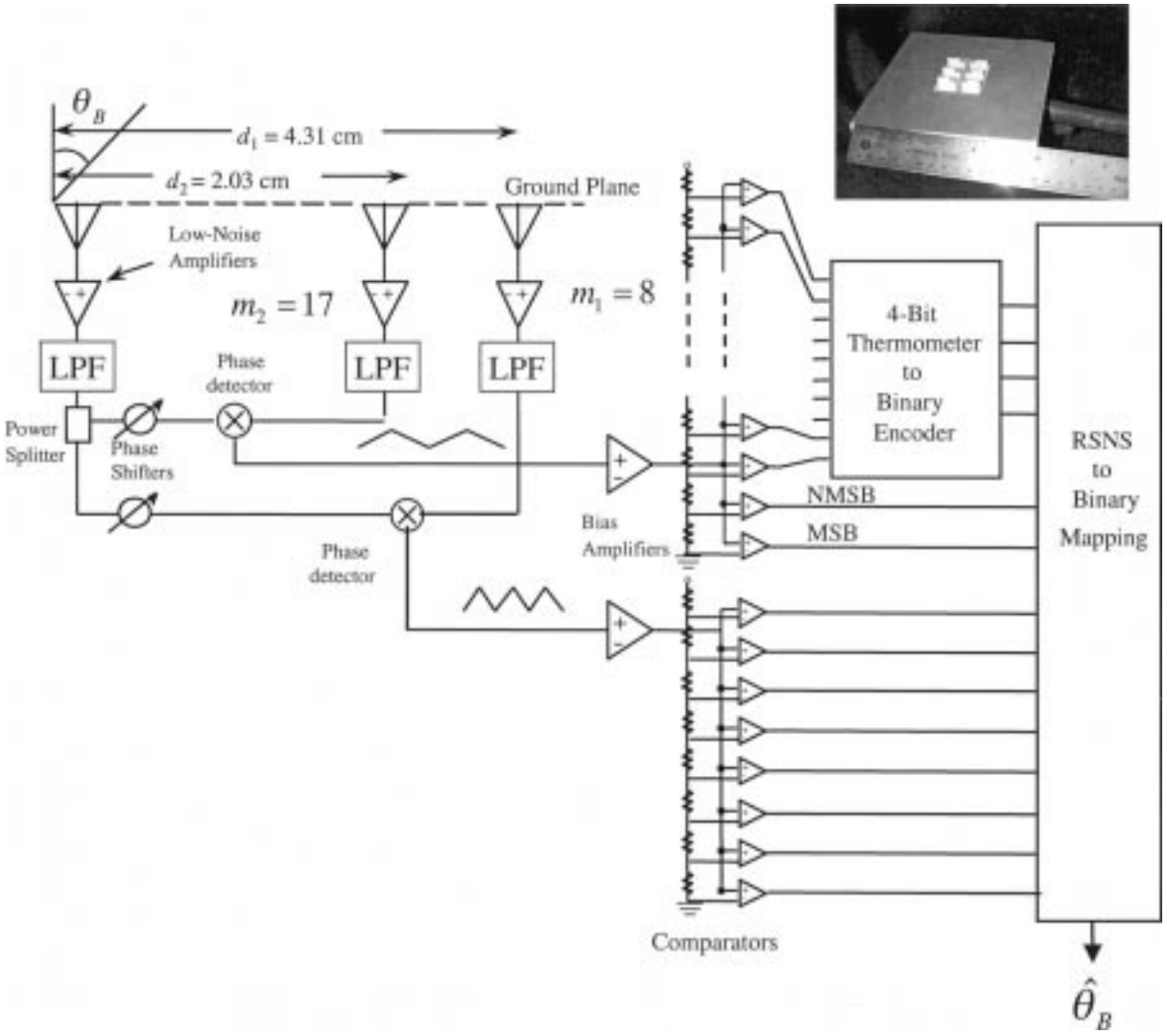

Fig. 8. Schematic diagram of the RSNS array with $m_1 = 8$ and $m_2 = 17$.

period for the RSNS vectors must be a multiple of $2Nm_i$. Therefore, the *fundamental period* for the RSNS is

$$PF_{\text{RSNS}} = [2m_1N, 2m_2N, \ldots, 2m_NN] \tag{16}$$

where $[a_1, a_2, \ldots, a_N]$ is the least common multiple of $a_1, a_2, \ldots, a_N$. From number theory [7]

$$PF_{\text{RSNS}} = 2N[m_1, m_2, \ldots, m_N]. \tag{17}$$

To illustrate the RSNS, Fig. 4(b) shows the folding waveform and integer values within each modulus for $m_1 = 5$ (shift $s_1 = 0$) $m_2 = 6$ (shift $s_2 = 1$). Note the Gray-code properties from one code transition to the next. The thresholds shown on the vertical axis represent the integer values within each RSNS modulus. The integer values occur $N = 2$ times in succession.

The *system dynamic range* ($\hat{M}_{\text{RSNS}}$) of the RSNS is the maximum number of distinct vectors without a redundancy. The performance of the 2-channel example is shown in Fig. 4(b). The selection of the shift and the permutations between the 2 moduli has no effect on $\hat{M}_{\text{RSNS}}$. However, the point indices corresponding to $\hat{M}_{\text{RSNS}}$ (beginning point and ending point) are different. When the channel moduli are of the form $m_1 = 2^k - 1$, $m_2 = 2^k$, $m_3 = 2^k + 1$, the closed-form expression for $\hat{M}_{\text{RSNS}}$ is conjectured to be

$$\hat{M}_{\text{RSNS}} = \tfrac{3}{2}m_1^2 + \tfrac{15}{2}m_1 + 7 \tag{18}$$

where $m_1 \geq 3$. For two channels, with the moduli separated by 3 or more

$$\hat{M}_{\text{RSNS}} = 4m_1 + 2m_2 - 2. \tag{19}$$

Checking against computer results when $m_1 = 8$ and $m_2 = 17$, $\hat{M} = 64$ which fits (19).

B. RSNS Antenna Design

To demonstrate the efficiency of the RSNS preprocessing, the design of a 6-bit antenna using $m_1 = 8$ and $m_2 = 17$ is considered. A schematic diagram of the RSNS antenna is shown in Fig. 8 for $s_1 = 0$, $s_2 = 1$ resolution bins. The number of folds within each modulus is

$$n_i = \frac{\hat{M}}{P_{\text{RSNS}}} = \frac{\hat{M}}{2m_iN} \tag{20}$$

Vector	Mod 8	Mod 17	Bin	Vector	Mod 8	Mod 17	Bin	Vector	Mod 8	Mod 17	Bin
1	0	0		34	1	16	13	67	1	1	46
2	1	0		35	1	17	14	68	2	1	47
3	1	1		36	2	17	15	69	2	0	48
4	2	1		37	2	16	16	70	3	0	49
5	2	2		38	3	16	17	71	3	1	50
6	3	2		39	3	15	18	72	4	1	51
7	3	3		40	4	15	19	73	4	2	52
8	4	3		41	4	14	20	74	5	2	53
9	4	4		42	5	14	21	75	5	3	54
10	5	4		43	5	13	22	76	6	3	55
11	5	5		44	6	13	23	77	6	4	56
12	6	5		45	6	12	24	78	7	4	57
13	6	6		46	7	12	25	79	7	5	58
14	7	6		47	7	11	26	80	8	5	59
15	7	7		48	8	11	27	81	8	6	60
16	8	7		49	8	10	28	82	7	6	61
17	8	8		50	7	10	29	83	7	7	62
18	7	8		51	7	9	30	84	6	7	63
19	7	9		52	6	9	31	85	6	8	
20	6	9		53	6	8	32	86	5	8	
21	6	10	0	54	5	8	33	87	5	9	
22	5	10	1	55	5	7	34	88	4	9	
23	5	11	2	56	4	7	35	89	4	10	
24	4	11	3	57	4	6	36	90	3	10	
25	4	12	4	58	3	6	37	91	3	11	
26	3	12	5	59	3	5	38	92	2	11	
27	3	13	6	60	2	5	39	93	2	12	
28	2	13	7	61	2	4	40	94	1	12	
29	2	14	8	62	1	4	41	95	1	13	
30	1	14	9	63	1	3	42	96	0	13	
31	1	15	10	64	0	3	43	96	0	14	
32	0	15	11	65	0	2	44	97	1	14	
33	0	16	12	66	1	2	45	98	1	15	

Fig. 9. RSNS logic block.

or $n_1 = 2$, and $n_2 = 0.94$. The required distance between antenna elements is

$$d_i = n_i \frac{\lambda}{2} = \frac{\hat{M}\lambda}{4m_i N}\xi. \tag{21}$$

With a scale factor of $\xi = 2/\sqrt{3}$, $d_1 = 4.33$ cm, and $d_2 = 2.03$ cm. For a normalized folding waveform amplitude (-1 to 1), the threshold for the jth comparator for the modulus m_i channel is

$$V_{j,m_i} = \cos\left(\frac{m_i - j + \frac{1}{2}}{m_i}\,\pi\right). \tag{22}$$

The input signal is applied in parallel to both interferometers. The output from each phase detecting mixer is amplitude analyzed using m_i comparators. For this design, there are a total of 25 comparators with a maximum of 17 loaded in parallel. An RSNS-to-binary logic block translates the RSNS residues (number of comparators ON in each thermometer code) to a more convenient representation. The logic block and corresponding index n are shown in Fig. 9.

A consequence of quantizing the angle of arrival into a bin is that the RSNS system reports any signal that falls within a bin as if it arrived at the bin center, $\hat{\theta}_k$. That is to say, for one angle within each bin, the estimation is exact, but for the remaining angles a reporting error exists. The AOA resolution or bin width in *θ-space* for the kth bin is

$$r_k = \arcsin\left(\frac{2\mathrm{k} - \hat{\mathrm{M}} + 2}{\xi\hat{\mathrm{M}}}\right) - \arcsin\left(\frac{2\mathrm{k} - \hat{\mathrm{M}}}{\xi\hat{\mathrm{M}}}\right). \tag{23}$$

Another advantage of the RSNS is that small phase errors can be tolerated without a serious error to a reported AOA. These phase errors cause the folded waveform from the mixer to shift, thus, changing the timing of the comparator state changes. Because the waveforms from the mixers are quantized, the bin width or r_k provides some freeplay in the antenna circuitry and limits AOA reporting errors to the adjacent quantization levels (bins). However, there is a limit to this feature. If the phase error becomes too great, the comparators will not change state in the correct sequence, which may or may not correspond to a code that is mapped in the dynamic range. These errors are similar to the errors that the OSNS experiences when the comparators of both channels do not change state at the same time. For the system designed, a theoretical phase error of 6° can be tolerated in the modulus 17 channel and a phase error of 12° in the modulus 8 channel. Figs. 10 and 11(a) and (b) show the simulated transfer function. Fig. 10 is the transfer function with no phase error in both channels. Fig. 11(a) and (b) are the modulus 8 channel with zero degrees of phase error and 3° and 6° phase error in the modulus 17 channel. Note how the transfer function

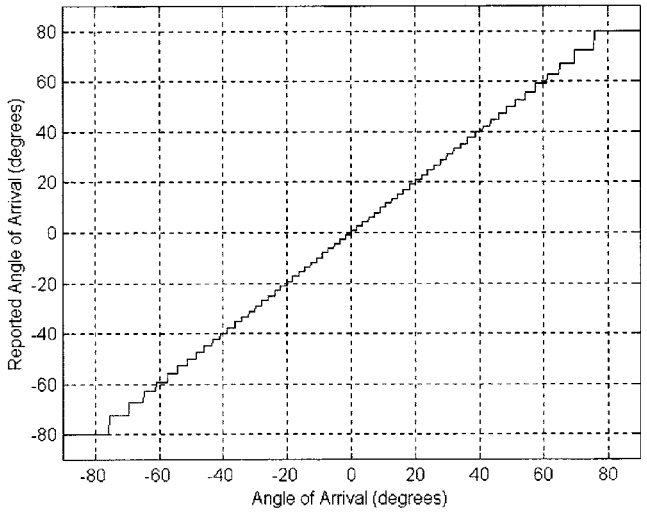

Fig. 10. Simulated transfer function with no phase errors in either channel.

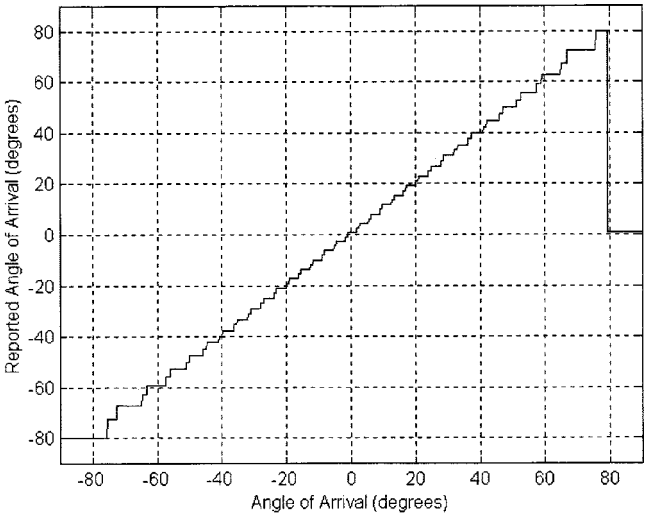

(a)

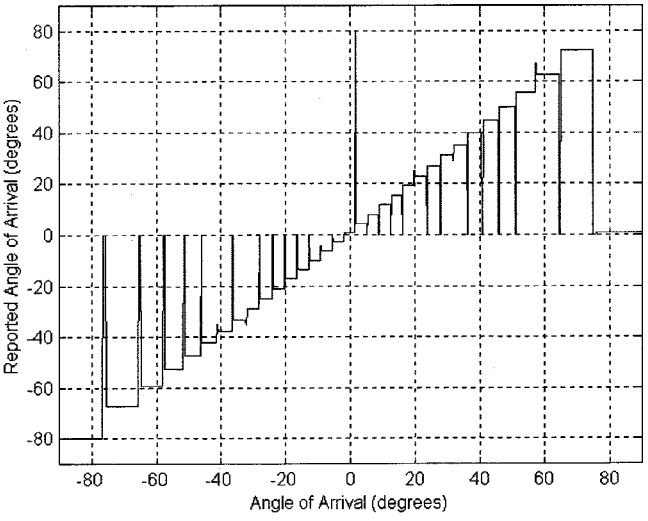

(b)

Fig. 11. Modulus 17 channel. (a) 3°. (b) 6° phase error introduced.

becomes jagged and erratic as the phase error is increased until it becomes discontinuous at 6°.

C. Experimental Results

A RSNS array based on the moduli $m_1 = 8$ and $m_2 = 17$ was designed, fabricated, and tested at a frequency of 8.0 GHz. The schematic diagram of the two-channel array is shown in Fig. 8. The radiating elements are printed circuit dipoles. For moduli $m_1 = 8$ and $m_2 = 17$, the unscaled distances, $\xi = 1$, are $d_1 = 3.76$ cm and $d_2 = 1.78$ cm. With $\hat{M} = 64$, the number of folding periods $n_1 = 2$ and $n_2 = 0.94$. To provide an adequate signal-to-noise ratio, a low-noise amplifier is included at the output of each interferometer element. Also included in the RSNS array is a lowpass filter in each channel to eliminate the amplifier harmonics that are present. Since the common element splits the signal into N paths, an attenuator is placed in the other branches to balance the amplitudes. A fixed-phase shifter is also included in one branch of each interferometer so that the symmetrically folded phase response waveforms from each mixer may be aligned. This alignment insures that the comparators in the digital processor properly sample the phase waveform and encode it in the RSNS. For the $m_1 = 8$ channel, 8 comparators are required. For the $m_2 = 17$ channel 17 comparators are required. The electrically erasable read only membory (EEPROM) that was used accommodates 15 inputs. The modulus 17 channel processing is conducted in two stages. In the first stage, the 4-bit thermometer to binary encoder maps the 15 least significant codes out of the 17 comparators (ones with the smallest threshold). The remaining two comparators are mapped on the second EEPROM along with the 4-bit binary encoder output and all modulus 8 comparators. The digital processor puts out a bin number k corresponding to the estimated AOA $\hat{\theta}$. The estimated AOA for bin k is given as

$$\hat{\theta}_k = \sin^{-1}\left(\frac{2k+1}{\xi \hat{M}} - \frac{1}{\xi}\right). \tag{24}$$

Broadside incidence for the RSNS antenna corresponds to the transition between Bins 31 and 32. For the modulus 17 channel, at slightly negative angles (bin 31), the ninth comparator is ON and for slightly positive angles (bin 32), the ninth comparator is OFF. That is, the phase value at $\theta_B = 0$ corresponds exactly to the threshold of the ninth comparator. From (22) the phase corresponding to the threshold value $V_{17,9}$ is $\pi/2$. This is the phase value required for the modulus 17 channel at $\theta_B = 0$ and is obtained using the phase adjuster shown in Fig. 8. In the modulus 8 channel, $\theta_B = 0$ occurs midway between comparator 7 and 6 thresholds. Since $V_{8,7} = \cos^{-1}(5\pi/16)$ and $V_{8,6} = \cos^{-1}(3\pi/16)$, the required phase value is $4\pi/16 = \pi/4$and is also obtained using the modulus 8 phase adjuster.

The normalized mixer folding waveform outputs are shown with the simulated waveforms in Fig. 12(a) for the $m_1 = 8$ channel and Fig. 12(b) for $m_2 = 17$ channel for $\xi = 1.0$ and the basic features correspond to predicted curves. The measured folding outputs from the shift and bias amplifiers in both channels are shown in Fig. 13. The digital circuit maps the phase difference at the mixer output into an estimated angle of arrival. The predicted output of the unscaled prototype array is reproduced as Fig. 14(a). The measured mixer output contains phase errors that result in differences between the simulated and predicted data. These phase errors cause the thermometer code to

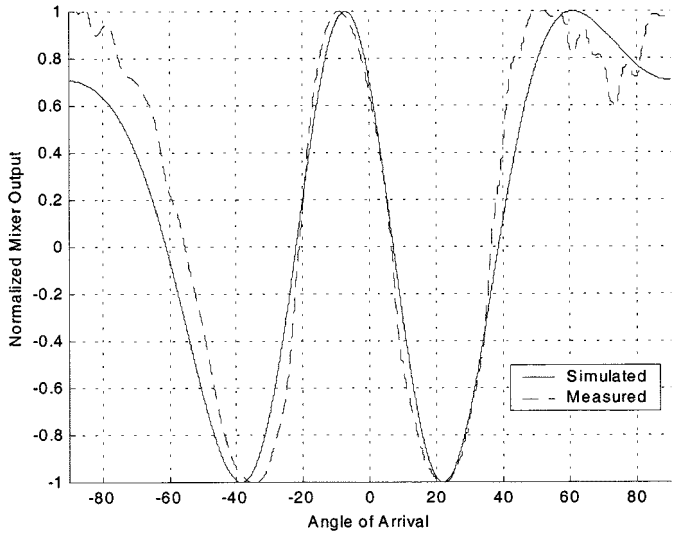

(a)

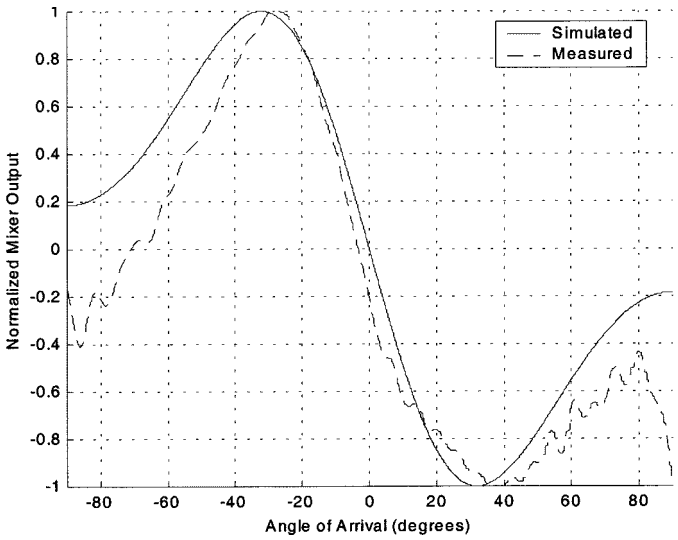

(b)

Fig. 12. Normalized mixer output and simulation waveforms for RSNS array. (a) $m_1 = 8$. (b) $m_2 = 17$.

incorrectly map the incident wave to the proper angle of arrival. The measured transfer function of the unscaled prototype antenna is shown in Fig. 14(b).

The large discontinuities in the transfer function are due to phase and amplitude errors that arise from several sources. Mutual coupling is a common cause of phase front distortion in small arrays of closely spaced elements. In order to increase the distance between elements and thus reduce the mutual coupling, a scale factor ξ can be introduced. The scale factor is the ratio of the element spacings of the scaled and unscaled arrays. Reducing the scale factor narrows the mapable field of view of the antenna and increases the resolution within the mapable field of view. For a scale factor of $\xi = 2/\sqrt{3}$, the maximum mapable aperture (θ_{MM}) is 60°. The predicted transfer function for the scaled array is shown in Fig. 15(a). The corresponding measured transfer function is reproduced as Fig. 15(b). The mixer outputs contain significant phase errors, and the increased resolution of the antenna limits the ability to process the errors. The steeper

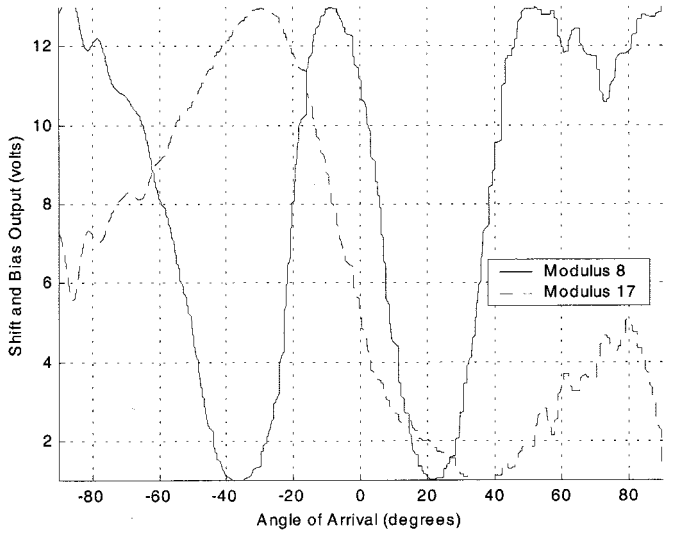

Fig. 13. Measured folding waveform outputs from the shift and bias amplifiers.

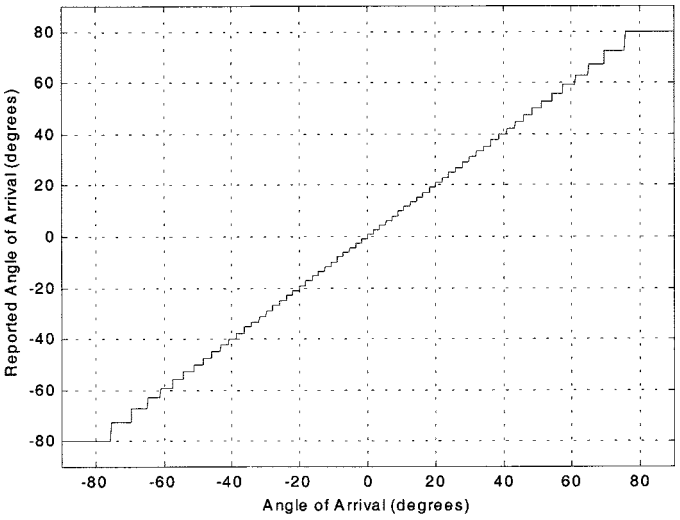

(a)

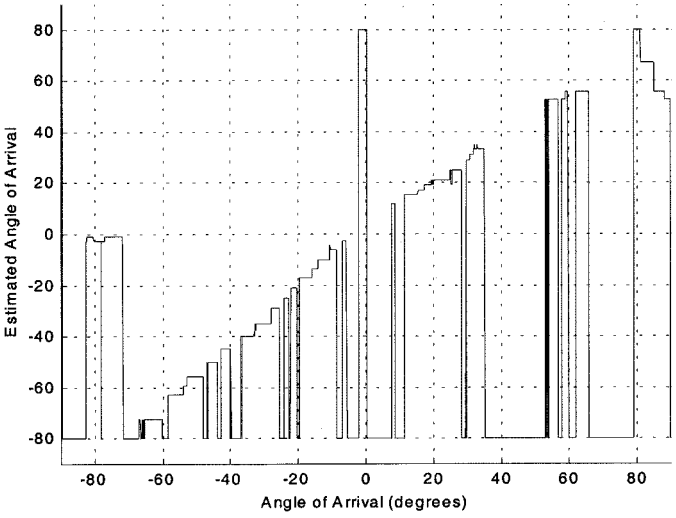

(b)

Fig. 14. RSNS transfer functions. (a) Predicted. (b) Measured.

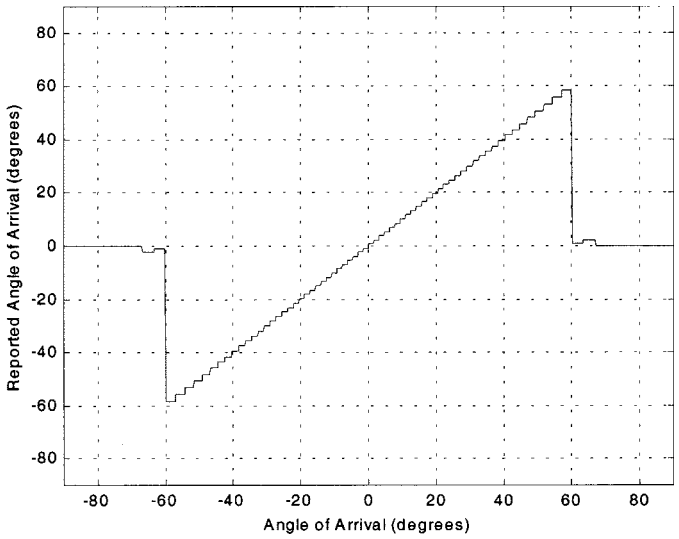

(a)

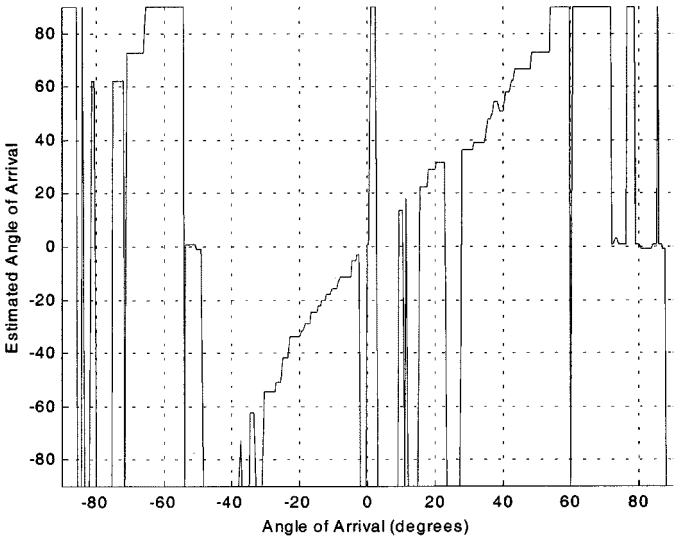

(b)

Fig. 15. RSNS transfer functions, scale factor $\xi = 2/\sqrt{3}$. (a) Predicted. (b) Measured.

slope of the scaled transfer function is clearly visible when comparing Figs. 14(a) and 15(a).

The transfer function for the scaled array of dipoles does not show any significant improvement due to the reduction of mutual coupling. To verify this, a second array comprised of open ended waveguide elements was constructed and tested. These waveguide elements have significantly less H-plane mutual coupling than the dipoles, but the transfer function showed no improvement over with printed circuit (dipole) elements. This indicates that mutual coupling is not the primary cause of the phase errors. The microwave circuit has three likely sources of errors: 1) The low noise amplifiers; 2) coaxial cables and phase adjusters; and 3) the rigid connectors. The prototype uses two cascaded LNAs operating in saturation in each channel. The second amplifier amplifies harmonics generated by the first amplifier. The second amplifier also introduces its own harmonics. Filters were used to suppress harmonics.

The coaxial cables and phase adjusters are another source of error within microwave circuits. The rigid coaxial cables are coarsely trimmed at 8.0 GHz and the phase shifters are used for fine trimming. The cable lengths are long and subject to thermal expansion and contraction, particularly in the vicinity of the amplifiers. Finally, all of the devices in the circuit are joined with SMA type connectors. The circuit was repeatedly assembled and disassembled for troubleshooting and consequently the quality of the connections was degraded. Phase errors of $\pm 2^\circ$ can easily be introduced at each connection. Thus, it appears that many small errors accumulate in a manner such that the 6° and 12° error thresholds are exceeded, resulting in a degraded transfer function.

V. Conclusion

This research has introduced the OSNS and the RSNS and shown they can be used to resolve ambiguities in phase sampling interferometry. A direction finding antenna architecture based on the OSNS has many inherent advantages over conventional direction finding techniques including: simple microwave beamforming network that incorporates wideband components, wide instantaneous field of view, and high resolution angle of arrival with a variety of element arrangements having very short baselines. The design equations for comparator thresholds, broadside phase difference, and a scale factor are derived. The simulated transfer functions demonstrate that the OSNS and RSNS antenna will have a wide instantaneous field of view and high resolution.

Test arrays were built and their performance measured. The measured transfer functions, while exhibiting the basic features of the ideal transfer function, contained significant encoding errors. The errors are attributed to phase errors in the microwave circuit and its components, as well as mutual coupling. Using a printed circuit design with surface mount components can reduce these errors significantly.

Acknowledgment

The authors would like to thank Prof. D. Styer for helpful comments and Mr. B. Vitale for his help in the anechoic chamber.

References

[1] E. Jacobs and E. W. Ralston, "Ambiguity resolution in interferometry," *IEEE Trans. Aerosp. Electron. Syst.*, vol. AES-17, Nov. 1981.

[2] Y. W. Wu, S. Rhodes, and E. H. Satorius, "Direction of arrival estimation via extended phase interferometry," *IEEE Trans. Aerosp. Electron. Sys.*, vol. 31, pp. 375–382, Jan. 1995.

[3] D. Peavy and T. Ogumfunmi, "The single channel interferometer using a pseudo-doppler direction finding system," *IEEE Trans. Acoust., Speech, Signal Processing*, pp. 4129–4132, 1997.

[4] W. A. U. Titze, P. V. Brennan, and R. Benjamin, "Direction finding system using symmetric-pair antenna arrays," in *Inst. Elect. Eng. Proc. Radar, Sonar, Navigation*, vol. 142, June 1995, pp. 130–136.

[5] P. E. Pace, J. L. Schafer, and D. Styer, "Optimum analog preprocessing for folding ADC's," *IEEE Trans. Circuits Syst. II*, vol. 42, pp. 825–829, Dec. 1995.

[6] P. E. Pace and D. Styer, "High-resolution encoding process for an integrated optical analog-to-digital converter," *Opt. Eng.*, vol. 33, pp. 2638–2645, Aug. 1994.

[7] P. E. Pace, D. Styer, and I. A. Akin, "A folding ADC preprocessing architecture employing a robust symmetrical number system with Gray-code properties," *IEEE Trans. Circuits. Syst. II*, vol. 47, pp. 462–467, May 2000.

Phillip E. Pace (S'87–M'90–SM'97) received the B.S. and M.S. degrees from The Ohio State University, Columbus, in 1983 and 1986, respectively, and the Ph.D. from the University of Cincinnati, OH, 1990, all in electrical and computer engineering.

He is a Professor in the Department of Electrical and Computer Engineering at the Naval Postgraduate School (NPS), Monterey, CA. Prior to joining NPS, he was with General Dynamics Corporation, Air Defense Systems Division, as a design specialist in the Radar Systems Research Engineering department for two years. Prior to his position with General Dynamics, he was with Hughes Aircraft Company, Radar Systems Group, as a member of the technical staff for five years. He has been a Principal Investigator with numerous research projects in the areas of optical signal processing, electronic warfare, and weapon systems analysis

Dr. Pace recieved the Outstanding Research Achievement Award in 1994 and 1995 for his work at the Naval Postgraduate School in electronic warfare. In 1995, he received the Association of Old Crows Academic Training Award. Since 1998, he has been Chairman of the Navy's Threat Simulator Validation Working Group 8 and was a participant on the Navy's NULKA Blue Ribbon Panel in January, 1999. He is the author of the textbook *Advanced Techniques for Digital Receivers*, (Artech House: Norwood, MA, 2000) and and is a member of the SPIE and AOC.

David Wickersham, received the B.S.M.E. from the United States Naval Academy, Annapolis, MD, in 1992. He received the Masters degree in applied physics from the Naval Postgraduate School, Monterey, CA, in March 2000.

He was simultaneously commissioned an Ensign in the United States Navy and reported to the Naval Nuclear Power School. He has served as Reactor Controls Division Officer onboard the U.S.S. BAINBRIDGE (CGN-25) and as Fire Control Officer onboard U.S.S. DAVID R. RAY (DD-971). He is presently, Operations Officer on U.S.S. ARTHUR W. RADFORD (DD-968).

David C. Jenn (S'75–M'79–SM'93) received the Ph.D. degree in electrical engineering from the University of Southern California in 1987.

From 1976 to 1978 he was with McDonnell Douglas Astronautics Co., St. Louis, MO, where he was involved in the design of small arrays and radomes for airborne platforms. In 1978 he joined Hughes Aircraft Company, where he concentrated on the design and analysis of high-performance phased array antennas for radar and communication systems and radar cross section analysis. In 1990, he joined the Department of Electrical and Computer Engineering at the Naval Postgraduate School as an Associate Professor. Since then he has continued his work on the application of the method of moments to array and reflector antenna design, as well as scattering by complex bodies. He is author of the book *Radar and Laser Cross Section Engineering* (AIAA, Washington, DC, 1995).

Dr. Jenn is a Member of the American Institute of Aeronautics and Astronautics (AIAA), Tau Beta Pi, American Society for Engineering Education (ASEE), the Society of Optical Engineers (SPIE) and the Applied Computational Electromagnetics Society (ACES).

Nathan S. York was born in Standish, MA, in 1970. He received the B.S. degree in civil engineering from the Worcester Polytechnic Institute, MA, in 1994. He received the M.S. degree in applied physics from the Naval Postgraduate School, Monterey, CA, in 2000

From 1994 to 1998, he served aboard U.S.S. CLARK (FFG-11) as 1st Lieutenant and Ordnance Officer, where he earned his Surface Warfare Officer qualification, and aboard U.S.S. PENSACOLA (LSD-38) as Combat Information Center Officer from 1996 to 1998. He currently attends the Department Head School in Newport, RI, in route to the U.S.S. BRISCOE (DD-977) as the Combat Systems Officer.

LT. York is a member of the American Society of Naval Engineers.